Article

# Enzyme Control of Small-Molecule Coordination in FosA as Revealed by P Pulsed ENDOR and ESE-EPR

Charles J. Walsby, Joshua Telser, Rachel E. Rigsby, Richard N. Armstrong, and Brian M. Hoffman

*J. Am. Chem. Soc.*, **2005**, 127 (23), 8310-8319• DOI: 10.1021/ja044094e • Publication Date (Web): 20 May 2005



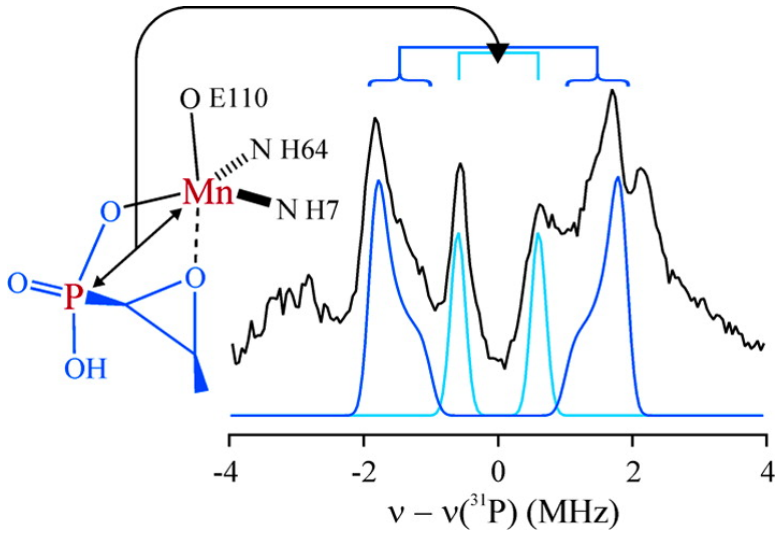


## More About This Article

Additional resources and features associated with this article are available within the HTML version:

- Supporting Information
- Links to the 4 articles that cite this article, as of the time of this article download
- Access to high resolution figures
- Links to articles and content related to this article
- Copyright permission to reproduce figures and/or text from this article

View the Full Text HTML

J|A|C|S
ARTICLES
Published on Web 05/20/2005

# Enzyme Control of Small-Molecule Coordination in FosA as Revealed by $^{31}$P Pulsed ENDOR and ESE-EPR

Charles J. Walsby,[†,§] Joshua Telser,[†,||] Rachel E. Rigsby,[‡] Richard N. Armstrong,[‡] and Brian M. Hoffman*[,†]

*Contribution from the Department of Chemistry, Northwestern University, 2145 Sheridan Road, Evanston, Illinois 60208-3113, and Departments of Biochemistry and Chemistry, Vanderbilt University, Nashville, Tennessee 37232-0146*

Received September 28, 2004; E-mail: bmh@northwestern.edu

***Abstract:*** FosA is a manganese metalloglutathione transferase that confers resistance to the broad-spectrum antibiotic fosfomycin, which contains a phosphonate group. The active site of this enzyme consists of a high-spin $Mn^{2+}$ ion coordinated by endogenous ligands (a glutamate and two histidine residues) and by exogenous ligands, such as substrate fosfomycin. To study the $Mn^{2+}$ coordination environment of FosA in the presence of substrate and the inhibitors phosphonoformate and phosphate, we have used $^{31}$P pulsed electron−nuclear double resonance (ENDOR) at 35 GHz to obtain metrical information from $^{31}$P−$Mn^{2+}$ interactions. We have found that continuous wave (CW) $^{31}$P ENDOR is not successful in the study of phosphates and phosphonates coordinated to $Mn^{2+}$. Parallel studies of phosph(on)ate binding to the $Mn^{2+}$ of FosA and to aqueous $Mn^{2+}$ ion disclose how the enzyme modifies the coordination of these molecules to the active site $Mn^{2+}$. Through analysis of $^{31}$P hyperfine parameters derived from simulations of the ENDOR spectra we have determined the binding modes of the phosph(on)ates in each sample and discerned details of the geometric and electronic structure of the metal center. The $^{31}$P ENDOR studies of the protein samples agree with, or improve on, the Mn−P distances determined from crystal structures and provide Mn−phosph(on)ate bonding information not available from these studies. Electron spin echo electron paramagnetic resonance (ESE-EPR) spectra have also been recorded. Simulation of these spectra yield the axial and rhombic components of the $Mn^{2+}$ ($S = {}^5/_2$) zero-field splitting (zfs) tensor. Comparison of structural inferences based on these zfs parameters both with the known enzyme structures and the $^{31}$P ENDOR results establishes that the time-honored procedure of analyzing $Mn^{2+}$ zfs parameters to describe the coordination environment of the metal ion is not valid or productive.

## Introduction

The FosA group of fosfomycin resistance proteins catalyzes the addition of glutathione to carbon-1 of the broad-spectrum antibiotic fosfomycin ((1*R*,2*S*)-epoxypropylphosphonic acid) to yield 1-(*S*-glutathionyl)-2-hydroxypropylphosphonic acid, rendering it inactive (Scheme 1, where GSH is glutathione).[1−3] Both plasmid and genomically encoded versions of FosA are capable of conferring clinically significant resistance to the antibiotic in pathogenic microorganisms.[4]

***Scheme 1***

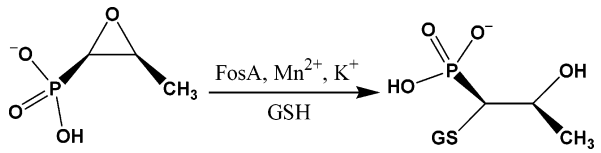


Biochemical and spectroscopic studies of the plasmid-encoded enzyme have demonstrated that a $Mn^{2+}$ center is directly involved in catalysis and that $K^+$ is required for optimal activity.[2,3,5−7] Mutagenesis and sequence alignment experiments have identified H7, H64, and E110 as the protein ligands.[3,5] Electron paramagnetic resonance (EPR) experiments first demonstrated the binding of fosfomycin and $PO_4$ to the active site

[†] Northwestern University.
[‡] Vanderbilt University.
[§] Current address: Department of Chemistry, Simon Fraser University, 8888 University Drive, Burnaby, British Columbia V5A 1S6 Canada.
[||] Permanent address: Chemistry Program, Roosevelt University, Chicago, IL 60605-1394.

(1) Abbreviations used: DTT, 1,4-dithio-DL-threitol; ESEEM, electron spin−echo envelope modulation; FosA, fosfomycin resistance protein (fosfomycin is (1*R*,2*S*)-epoxypropylphosponic acid); TMA-HEPES, tetramethylammonium 4-(2-hydroxyethyl)piperazine-1-ethanesulfonic acid. Symbols used: $A_{iso}$, isotropic hyperfine interaction; E·$Mn^{2+}$·X, without indication of the enzymes' origin is genomically encoded FosA (PA1129) from *P. aeruginosa*, where X = S (fosfomycin), Pf (phosphonoformate), $PO_4$ (in phosphate buffer); $Mn^{2+}$·X is frozen aqueous $MnCl_2$ solutions, where X = S, Pf, $PO_4$; *T*, anisotropic hyperfine interaction; $T_{loc}$, through-space interaction with spin density in the local orbitals that is derived from through-bond interaction with the paramagnetic center; $T_{non-loc}$, nonlocal, through-space contribution to anisotropic hyperfine coupling.

(2) Arca, P.; Rico, M.; Brana, A. F.; Villar, C. J.; Hardisson, C.; Suarez, J. E. *Antimicrob. Agents Chemother.* **1988**, *32*, 1552−1556.
(3) Bernat, B. A.; Laughlin, L. T.; Armstrong, R. N. *Biochemistry* **1997**, *36*, 3050−3055.
(4) Rife, C. L.; Pharris, R. E.; Newcomer, M. E.; Armstrong, R. N. *J. Am. Chem. Soc.* **2002**, *124*, 11001−11003.
(5) Bernat, B. A.; Laughlin, L. T.; Armstrong, R. N. *Biochemistry* **1999**, *38*, 7462−7469.
(6) Bernat, B. A.; Armstrong, R. N. *Biochemistry* **2001**, *40*, 12712−12718.
(7) Smoukov, S. K.; Telser, J.; Bernat, B. A.; Rife, C. L.; Armstrong, R. N.; Hoffman, B. M. *J. Am. Chem. Soc.* **2002**, *124*, 2318−2326.


**10.1021/ja044094e CCC: $30.25** 

$Mn^{2+}$ of FosA (from transposon TN2921), and analysis of the zero-field splitting (zfs) parameters determined from these spectra led to conclusions regarding the symmetry of the $Mn^{2+}$ coordination environment through analysis of the zfs parameters.[7] The above results have largely been confirmed by the recent publication of the crystal structures of the genomically encoded FosA (PA1129) from *Pseudomonas aeruginosa* in which the $Mn^{2+}$ ion is coordinated by $PO_4$,[4] substrate fosfomycin,[4] and inhibitor phosphonoformate.[8] These structures of FosA with phosphate, fosfomycin, and phosphonoformate were determined at 1.35, 1.19, and 0.95 Å resolution, respectively, from data collected at 113 K. The crystal structure of a $Mn^{2+}$ enzyme with coordinated phosphate shows the $Mn^{2+}$ to be four-coordinate with a highly distorted tetrahedral geometry, while coordination of fosfomycin produces a $Mn^{2+}$ "very close" to five-coordinate with nearly perfect trigonal bipyramidal geometry with a phosphonate oxygen in the plane and the oxirane oxygen located at one of the apical sites.[4] The coordination of the phosphonoformate inhibitor likewise produces a five-coordinated $Mn^{2+}$, but the fifth ligand in this case is supplied by a formate oxygen.[8]

Metal−phosphate coordination is abundant in nature, and general methods for its investigation are highly desirable. We report here the use of $^{31}P$ pulsed electron−nuclear double resonance (ENDOR) techniques at 35 GHz to probe the direct coordination of the substrate fosfomycin and the inhibitors phosphonoformate and $PO_4$ to both FosA and $Mn^{2+}$ in aqueous solution. The $^{31}P$ hyperfine couplings disclose the differences in $Mn^{2+}$−O−P bonding and phosphate speciation in solution and in the enzyme. Comparison of the results from electron spin echo (ESE) and continuous wave (CW) EPR at 35 GHz with the known enzyme structures and the $^{31}P$ ENDOR results establishes that the procedure of analyzing $Mn^{2+}$ zfs parameters to describe the coordination environment of the metal ion, while long in history, is short in utility.

## Experimental Section

**Preparation of Protein Samples. (a) Cloning, Expression, and Characterization of FosA from *P. aeruginosa*.** The construction of the expression vector and expression of the protein was as previously described.[4] Bacteria were lysed by sonication, and protein was purified by anion exchange chromatography as follows. Crude protein was dialyzed in 20 mM Tris, pH 7.5, plus 1 mM DTT (Buffer A) and then passed through a diethylaminoethyl (DEAE) column equilibrated with 20 mM Tris, pH 7.5. Protein was eluted with a 20−500 mM NaCl gradient. Further dialysis in buffer A containing 3 g of Chelex 100 resin and 5 mM EDTA followed by dialysis in buffer A provided a metal-free protein solution. The protein was then loaded onto a HiPrepQ column equilibrated with 20 mM Tris pH 7.5 and eluted with a 0−120 mM NaCl gradient using an FPLC system. Protein was then dialyzed in 20 mM $KH_2PO_4$, pH 6.8, plus 1 mM DTT and loaded onto a hydroxyapatite column equilibrated with 20 mM $KH_2PO_4$, pH 6.8. The protein was eluted by washing with the equilibration buffer. Purity was confirmed using SDS-PAGE. Protein was then dialyzed in 20 mM TMA-HEPES, pH 8.0 (Buffer B), plus 1 mM DTT, 3 g of Chelex, and 5 mM EDTA followed by dialysis in buffer B. Protein was then concentrated and stored in aliquots at −80 °C.

**(b) Potassium-Free Purification.** Protein was expressed and purified as described above until after the HiPrepQ column. Protein was then concentrated to 10 mg/mL and dialyzed in 20 mM Tris, pH 7.5, containing 100 mM NaCl and 100 $\mu$M EDTA (buffer C) plus 1 mM DTT. Protein was passed through an S100 column equilibrated with buffer C and eluted with an isocratic gradient of buffer C. Purity was confirmed using SDS-PAGE. Protein was then dialyzed in 20 mM TMA-HEPES, pH 8.0 (Buffer B), plus 1 mM DTT, 3 g of Chelex, and 5 mM EDTA followed by dialysis in buffer B. Protein was then concentrated and stored in aliquots at −80 °C.

**Preparation of Aqueous $Mn^{2+}$ Samples.** Aqueous solutions of $Mn^{2+}$·Pf, $Mn^{2+}$·S (Pf = phosphonoformate, S = fosfomycin) were prepared in 20 mM TMA-HEPES buffer, pH 8, with 500 $\mu$M $MnCl_2$, 100 mM KCl, 1mM Pf or S. $Mn^{2+}$·$PO_4$ was prepared with phosphate buffer at pH 8.

**Pulsed/CW EPR and Pulsed ENDOR.** The 35 GHz pulsed and CW EPR/ENDOR spectrometers have been described previously.[9,10] Both instruments are equipped with helium immersion dewars, and all measurements were carried out at approximately 2 K. The EPR spectra from each exhibit absorption line shapes rather than the first derivatives yielded by conventional slow-passage field-modulated EPR. In our CW 100 kHz field modulated experiments, absorption line shapes arise because adiabatic rapid-passage conditions[11] are obtained at the temperature and microwave powers used in these studies; in discussing the microwave power dependence of these spectra we specify the attenuation of the output of the Gunn diode,[12] whose nominal output is 100 mW.

Electron spin echo EPR (ESE-EPR) measurements employed a two-pulse Hahn ESE sequence ($t_p-\tau-2t_p-\tau-$echo), which produces an absorption-display spectrum.[13] The intensity of the spin−echo at a given field depends on $\tau$ and the applied microwave pulse power and duration ($t_p$). Ordinarily, these are jointly varied so as to achieve the maximum echo intensity (at $g \approx 2$ here), where the EPR envelope is maximal, with the constraint that the echo shape (echo intensity versus time after the second pulse) is undistorted; in this case the microwaves nominally rotate the electron spins by $\pi/2$ and the echo approximates to a single Gaussian. For completeness, we also explored the effects of deviating from these constraints (i.e., by use of higher powers and/or longer pulses) on the ESE-EPR spectrum of E·$Mn^{2+}$·S, the sample of greatest biochemical interest and with the richest 35 GHz EPR spectrum.

For high-spin $Mn^{2+}$ ($S = {}^5/_2$), the spectrum is dominated by the fine-structure interaction, described by axial ($D$) and rhombic ($E$) zfs parameters. The slow-passage, derivative presentation discriminates against broad features arising from the outer fine-structure transitions $\pm{}^5/_2 \leftrightarrow \pm{}^3/_2$, $\pm{}^3/_2 \leftrightarrow \pm{}^1/_2$ of the high-spin $Mn^{2+}$, and usually only the innermost $\pm{}^1/_2 \leftrightarrow \mp{}^1/_2$ fine-structure transition is detected. In contrast, optimized absorption-display spectra, whether via pulsed (ESE) or CW rapid-passage methods, show all of the $|\Delta M_S| = 1$ transitions clearly and thus allow far better determination of the zfs parameters.

**Pulsed ENDOR.** The pulsed ENDOR experiments used the Davies microwave pulse sequence ($\pi-T-\pi/2-\tau-\pi-\tau-$echo) where the radio frequency (RF) is applied during the interval T.[13] For both E·$Mn^{2+}$·$PO_4$ and E·$Mn^{2+}$·Pf, low signal intensities required that the applied RF bandwidth be broadened by mixing with 100 kHz noise to improve the sensitivity.[14] Selected measurements without noise mixing demonstrated that the ENDOR line shapes of the $MnCl_2$ frozen solutions were not affected. In the case of E·$Mn^{2+}$·S, resolution was significantly enhanced without noise broadening, while satisfactory signal-to-noise (S/N) was still possible.

(8) Rigsby, R. E.; Rife, C. L.; Fillgrove, K. L.; Newcomer, M. E.; Armstrong, R. N. *Biochemistry* **2004**, *43*, 13666−13673.
(9) Davoust, C. E.; Doan, P. E.; Hoffman, B. M. *J. Magn. Reson.* **1996**, *119*, 38−44.
(10) Werst, M. M.; Davoust, C. E.; Hoffman, B. M. *J. Am. Chem. Soc.* **1991**, *113*, 1533−1538.
(11) Mailer, C.; Hoffman, B. M. *J. Phys. Chem.* **1976**, *80*, 842−846.
(12) Hyde, J. S.; Newton, M. E.; Strangeway, R. A.; Camenisch, T. G.; Froncisz, W. *Rev. Sci. Instrum.* **1991**, *62*, 2969−2975.
(13) Schweiger, A.; Jeschke, G. *Principles of Pulse Electron Paramagnetic Resonance*; Oxford University Press: Oxford, U.K., 2001.
(14) Hoffman, B. M.; DeRose, V. J.; Ong, J. L.; Davoust, C. E. *J. Magn. Res.* **1994**, *110*, 52−57.

For an electron-spin system with spin $S$, ENDOR spectra are a superposition of signals from all of the $\Delta M_S = \pm 1$ transitions that have intensity at a particular magnetic field position. For an $I = {}^1/_2$ nucleus, the nuclear transitions associated with electronic fine-structure levels, $|M_S|$, have ENDOR frequencies given by:

$$\nu_{\pm}(M_S) = \nu_N \pm (2|M_S|)A/2 \quad (1)$$

where $\nu_N$ is the Larmor frequency and $A$ is the orientation-dependent hyperfine coupling constant.

In principle, ENDOR signals from any hyperfine coupled nucleus with $I > 0$ are observable. In practice, this is not always the case. This study focuses on ENDOR signals observed for $^{31}$P ($I = {}^1/_2$, isotopic abundance = 100%) from exogenous substrate and inhibitors. Signals from $^1$H were also readily observed, but not extensively investigated as these arise from a combination of exogenous and endogenous sources. Surprisingly, although the active site of FosA comprises $Mn^{2+}$ directly coordinated by histidine nitrogen,[4,8] no signals assignable to $^{14}$N ($I = 1$, 99.63%) were observed by pulsed or CW 35 GHz ENDOR; however, spectroscopic efforts in this area were not extensive. It was not deemed useful to employ X-band ESEEM measurements to examine the histidyl $^{14}$N, as their coordination had been disclosed by X-ray diffraction,[4,8] and at X-band, the EPR signal for E·$Mn^{2+}$·S is unfavorable for any advanced techniques.[7]

## Results

Genomically encoded FosA (PA1129) from *P. aeruginosa* is the subject of this study, rather than the TN2921 enzyme examined before,[7] and the notation E·$Mn^{2+}$·X without qualification will refer to this enzyme, with X = S (fosfomycin), Pf (phosphonoformate), $PO_4$ (in phosphate buffer). The FosA solutions described here all contained potassium ion (100 mM), which is required for enzyme function.[5] However, no differences were seen when $K^+$ was absent. Parallel experiments were also conducted on frozen aqueous solutions of $MnCl_2$ with added X, denoted $Mn^{2+}$·X.

**ESE-EPR of $Mn^{2+}$·X and of E·$Mn^{2+}$·X.** The 35 GHz ESE-EPR spectra of all three $Mn^{2+}$·X (X = S, Pf, $PO_4$) exhibit an intense absorption envelope centered at $g = 2.0$ (Figure 1), with a sharp central sextet arising from hyperfine splittings by $^{55}$Mn ($I = {}^5/_2$, isotopic abundance 100%) of the $|S, M_S\rangle = |{}^5/_2, \pm{}^1/_2\rangle \leftrightarrow |{}^5/_2, \mp{}^1/_2\rangle$ transitions; this sextet is readily observed in conventional slow-passage derivative-display EPR spectra. The "wings" of the spectra in Figure 1 arise from transitions that involve the other $M_S$ states. These absorption-display ESE-EPR spectra and rapid-passage CW-EPR spectra (not shown) of the $Mn^{2+}$·X are almost indistinguishable; they are significantly broadened compared to that of $Mn^{2+}$ in aqueous solution because the zfs parameters are larger. Simulations indicate an axial zfs parameter of $|D| \approx 0.03$ cm$^{-1}$ for all $Mn^{2+}$·X, with negligible rhombic distortion ($E$).[7]

In contrast, the ESE-EPR spectra of E·$Mn^{2+}$·X exhibit significant intensity outside the $g = 2.0$ region, extending to fields as low as ~1500 G for X = S. The features in the these spectra can be assigned to allowed transitions ($|\Delta M_S| = 1$) as indicated in Figure 1. We have simulated the ESE-EPR spectra of E·$Mn^{2+}$·X to determine their zfs parameters, which are collected in notes to Table 1. The 35 GHz rapid-passage CW EPR spectra of E·$Mn^{2+}$·X shown in Figures S1−S4 are similar, but not identical, to the corresponding ESE-EPR spectra. These differences will be discussed below.

The ESE-EPR spectra of E·$Mn^{2+}$ and E·$Mn^{2+}$·$PO_4$ are almost indistinguishable except that with the latter there is a slight increase in the relative intensity of the $|M_S| = {}^1/_2$ (Figure 1) fine-structure transition. In both cases, the "perpendicular" feature of the fine-structure interaction is resolved for the outer transitions and readily assigned, as shown; the spectra are simulated very well using the parameters $|D| = 0.105(5)$ cm$^{-1}$ and $|E| = 0.020(5)$ cm$^{-1}$ for both (Figure S5). The spectrum of E·$Mn^{2+}$·Pf has somewhat better resolution of the perpendicular components of the fine-structure interaction, but has similar splittings and comparable zfs parameters: $|D| = 0.090(5)$ cm$^{-1}$ and $|E| = 0.003(1)$ cm$^{-1}$ (Figure S5). The ESE-EPR spectrum of E·$Mn^{2+}$·S has greater breadth (signals at low field), which indicates a larger value of $D$, and extra splittings due to a significant rhombic distortion of the zfs (Figures 1, S4); simulation gives zfs parameters $|D| = 0.235(5)$ cm$^{-1}$ and $|E| = 0.022(1)$ cm$^{-1}$ (Figure S5). The intensities as calculated do not include any special linewidth broadening effects to mimic variations in relaxation time as a function of $M_S$ or other distortions. Thus, the good match between experiment and simulation in terms of intensity, as well as resonance position, confirms that the ESE-EPR spectrum is undistorted.

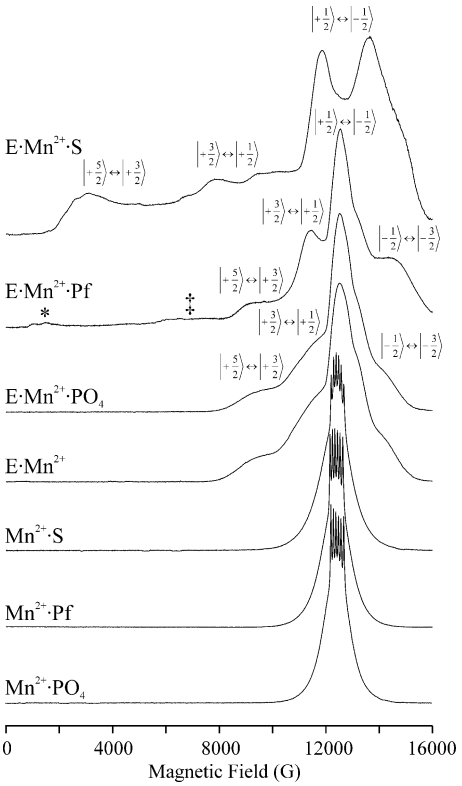


***Figure 1.*** ESE-EPR of FosA and $Mn^{2+}$ complexes. Pulse lengths 80 and 160 ns, interpulse time 460 ns, $T = 2$ K, 1024 points/scan, scan time = 500 s. Microwave frequencies (GHz): E·$Mn^{2+}$·S, 34.837; E·$Mn^{2+}$·Pf, 34.843; E·$Mn^{2+}$·$PO_4$, 34.850; E·$Mn^{2+}$, 34.813; $Mn^{2+}$·S, 34.931; $Mn^{2+}$·Pf, 34.840; $Mn^{2+}$·$PO_4$, 34.853. Non-Kramers EPR signal from a very small component of Mn(III) arising from a minimal amount of oxidation is indicated by the asterisk (*). Intensity from a forbidden transition, which is not suppressed even at extremely low power, is indicated by the double dagger (‡).

**CW versus ESE-EPR of E·$Mn^{2+}$·X.** The earlier EPR study highlighted the differences between the appearance of conventional, slow-passage, derivative-display EPR spectra and that of rapid-passage, absorption-display rapid-passage CW EPR spectra, demonstrating that the latter are substantially more informative in the case of high-spin $Mn^{2+}$.[7] Here, we compare

***Table 1.*** Simulation Parameters for $^{31}$P Hyperfine Couplings at $g \approx 2.0$ for $Mn^{2+}$ in FosA and Related Species[a]

| compound | $A_{iso}$ (MHz) | $T$ (MHz) | $T_{loc}$ (MHz) | $T_{non-loc}$ (MHz) | $r$(Mn–P) (Å) | linewidth (MHz) |
|---|---|---|---|---|---|---|
| $Mn^{2+}$·X, All Parameters from Simulation of ENDOR Data[b] | | | | | | |
| $Mn^{2+}$·$PO_4$ | 5.5(2) | 1.19 | 0.45 | 0.73 | 3.4(2) | 1.1 |
| $Mn^{2+}$·Pf | 2.2(1) | ≲0.35 | ≲0.18 | ≲0.17 | ≳5.6 | 1.1 |
| $Mn^{2+}$·S | 4.8(2) | 1.08 | 0.40 | 0.68 | 3.5(2) | 1.1 |
| E·$Mn^{2+}$·X, All Parameters from Simulation of ENDOR Data[c] | | | | | | |
| E·$Mn^{2+}$·$PO_4$ | 5.9(2) | ≲1.46 | ≲0.49 | ≲0.97 | ≳3.1 | 1.8 |
| E·$Mn^{2+}$·Pf | −3.2(2) | ≲1.63 | ≲−0.26 | ≲1.89 | ≳2.5 | 1.7 |
| E·$Mn^{2+}$·S[e] | −3.15(5) | 0.58 | −0.26 | 0.85 | 3.2(1) | 0.25 |
| E·$Mn^{2+}$·S[f] | 1.20(5) | ≲0.26 | ≲0.10 | ≲0.16 | ≳5.6 | 0.25 |
| E·$Mn^{2+}$·X, $T_{non-loc}$ Calculated from Crystal Structures[d] | | | | | | |
| E·$Mn^{2+}$·$PO_4$[g] | – | 2.58 | 0.50 | 2.08 | 2.49(3.25) | – |
| E·$Mn^{2+}$·Pf | −3.4(2) | 0.79 | −0.28 | 1.07 | 3.0 | 1.7 |
| E·$Mn^{2+}$·S[e] | −3.00(5) | 0.63 | −0.25 | 0.88 | 3.2 | 0.25 |
| E·$Mn^{2+}$·S[f] | 1.20(5) | 0.14 | 0.10 | 0.04 | 9.08 | 0.25 |

[a] Uncertainties were estimated by visual comparison of the experimental spectra with a series of simulations with varied parameters. The calculations of $r$(Mn−P) were made with the assumption of 90% spin localization on $Mn^{2+}$; the assumption of full spin localization on $Mn^{2+}$ would increase the ENDOR calculated distances by ∼0.1 Å. [b] The 35 GHz EPR spectra for all $Mn^{2+}$·X are essentially indistinguishable from that of $Mn^{2+}_{(aq)}$: $|D| \lesssim 0.03$ cm$^{-1}$, $E \approx 0$. [c] The 35 GHz EPR spectra for E·$Mn^{2+}$·X are dependent on X: none, $PO_4$: $|D| = 0.105(5)$ cm$^{-1}$, $|E| = 0.020(5)$ cm$^{-1}$; Pf: $|D| = 0.090(5)$ cm$^{-1}$, $|E| = 0.003(1)$ cm$^{-1}$; S: $|D| = 0.235(5)$ cm$^{-1}$, $|E| = 0.022(1)$ cm$^{-1}$. [d] Values of $A_{iso}$ for E·$Mn^{2+}$·X using $T_{non-loc}$ based on the values of $r$(Mn−P) from crystal structures were established by keeping $T_{non-loc}$ fixed and iteratively fitting $A_{iso}$ and $T$, since $T_{loc}$ is dependent on $A_{iso}$. [e] Values are given for the more strongly coupled signal, assigned as a coordinated substrate molecule (Figure 5). [f] Values are given for the less strongly coupled signal, assigned as a distant substrate molecule (Figure 5). [g] The crystal structure for the phosphate complex was refined with two partially occupied phosphate sites near the Mn in each subunit of the dimer: a primary site with occupancy 0.60 and a secondary site with occupancy 0.35. Use of the distance for the primary site, $r$(Mn−$^{31}$P) = 2.49 Å, gave a value of $T$ that was completely incompatible with the experimental ENDOR spectrum. However, the distances for the secondary site, $r$(Mn−$^{31}$P) = 3.33 Å for one subunit and 3.17 Å for the other (the average distance is given), are fully compatible with the ENDOR-derived distance.

and contrast the more subtle differences between rapid-passage CW EPR and ESE-EPR, both of which give absorption line shapes.

The rapid-passage CW EPR spectra at 2 K of the E·$Mn^{2+}$·X collected at very low microwave power (∼50 dB attenuation, ≲1 $\mu$W; Figures S2−S4) are almost indistinguishable from those of Figure 1. However, the CW spectra vary strongly with the applied microwave power. At higher microwave powers (≳1 $\mu$W at 2 K), the CW EPR spectra of E·$Mn^{2+}$·$PO_4$ and E·$Mn^{2+}$·Pf both exhibit features below ∼8000 G, Figures S2 and S3). The power dependence of these low-field peaks is consistent with their assignment as "forbidden" transitions ($|\Delta M_S| > 1$). Unfortunately, at the extremely low powers needed to prevent excitation of the forbidden transitions in the CW experiment, conditions for adiabatic rapid passage are not well met, leading to distortion of the spectra (see particularly Figure S3). Furthermore, the S/N is diminished relative to that at higher powers.

In contrast, it is relatively easy to choose pulse widths and powers that maximize the Hahn ESE intensity while maintaining proper echo shape (i.e., a single Gaussian). When this is done, the resulting ESE-EPR spectra have substantially better S/N than the low-power CW spectra; they do not show the forbidden transitions and are relatively straightforward to analyze.

For completeness, however, we have explored the consequences of deliberately mis-setting the pulse parameters on the ESE-EPR spectra. Interestingly, if the microwave pulse duration and/or power are increased beyond the optimum values, which correspond to $\pi/2$ spin mutation, as indicated by distorted echo shapes, then forbidden transitions become observable; in addition, the intensity of the allowed transitions is altered. These effects are demonstrated in Figure S6, which shows the dependence of the ESE-EPR spectrum of E·$Mn^{2+}$·S on pulse width and power and on $\tau$; the figure shows that an increase in pulse power by 6 dB corresponds exactly to an increase in pulse length by a factor of 2. It can be seen that only very high powers result in significantly distorted ESE-EPR spectra. The effect of delay time, $\tau$, is much less significant, provided that it neither becomes so short as to present "ring-down" problems (i.e., data sampling too soon after the microwave pulse) nor so long (≳1 $\mu$s) as to substantially reduce the echo intensity.

In summary, optimizing the intensity of the Hahn echo ESE-EPR signal automatically gives an undistorted EPR envelope and optimal S/N, whereas to acquire an undistorted CW spectrum requires low microwave powers that give low S/N.

**EPR of FosA from PA1129 (Genomically Encoded) versus TN2921 (Plasmid-Encoded).** The EPR spectra and analyses of E·$Mn^{2+}$·X (X = none, $PO_4$) in the present report differ from those of the previous study of the plasmid-encoded FosA from transposon TN2921, which employed only CW EPR in the study.[7] However, we have confirmed that E·$Mn^{2+}$·S, whether from TN2921 or PA1129, have very similar spectra and are simulated with zfs parameters (given above) that match, within experimental uncertainty.

The earlier spectra of E·$Mn^{2+}$ presented a pattern similar to those shown here for the frozen solutions $Mn^{2+}$·X, although with somewhat wider shoulders indicating larger $D$ and $E$. In contrast, as described above, CW and ESE-EPR measurements of PA1129 E·$Mn^{2+}$ have revealed a much broader pattern with resolution of the electron spin manifolds (Figure 1). Repeated preparation of this sample, with great care taken to exclude phosphate (the absence of which was confirmed using $^{31}$P ENDOR), lead us to conclude that the EPR spectra of E·$Mn^{2+}$ and E·$Mn^{2+}$·$PO_4$ from both TN2921 and PA1129 are all very similar and are simulated with the same zfs parameters (given above). There were several difficulties with the earlier study. First, the TN2921 FosA sample used in the earlier study was contaminated by excess unbound $Mn^{2+}$, and the earlier spectra were a composite of this signal plus the true E·$Mn^{2+}$ spectrum. Second, peaks seen below ∼8000 G for TN2921 E·$Mn^{2+}$·$PO_4$ were interpreted as $\Delta M_S = 1$ transitions for centers with a large zfs. However, the spectra were collected at relatively high CW microwave power, and the peaks in question should instead be assigned as $\Delta M_S > 1$ forbidden transitions, as discussed above. Finally, a peak close to zero field in the spectrum of TN2921 E·$Mn^{2+}$·$PO_4$ was not attenuated with reduced microwave power, and we suggest that this is a non-Kramers EPR signal from $Mn^{3+}$ ($S = 2$),[15] arising from an oxidized component in the protein sample. Similar signals are also observed with PA1129 E·$Mn^{2+}$·Pf (Figure S3).

**$^{31}$P ENDOR of $Mn^{2+}$·X and of E·$Mn^{2+}$·X.** Davies pulsed $^{31}$P ENDOR spectra were collected at fields corresponding to $g = 2.0$ for each of the samples and at the outer fine-structure transitions when resolved. Representative spectra for all six

(15) Campbell, K. A.; Yikilmaz, E.; Grant, C. V.; Gregor, W.; Miller, A.-F.; Britt, R. D. *J. Am. Chem. Soc.* **1999**, *121*, 4714−4715.

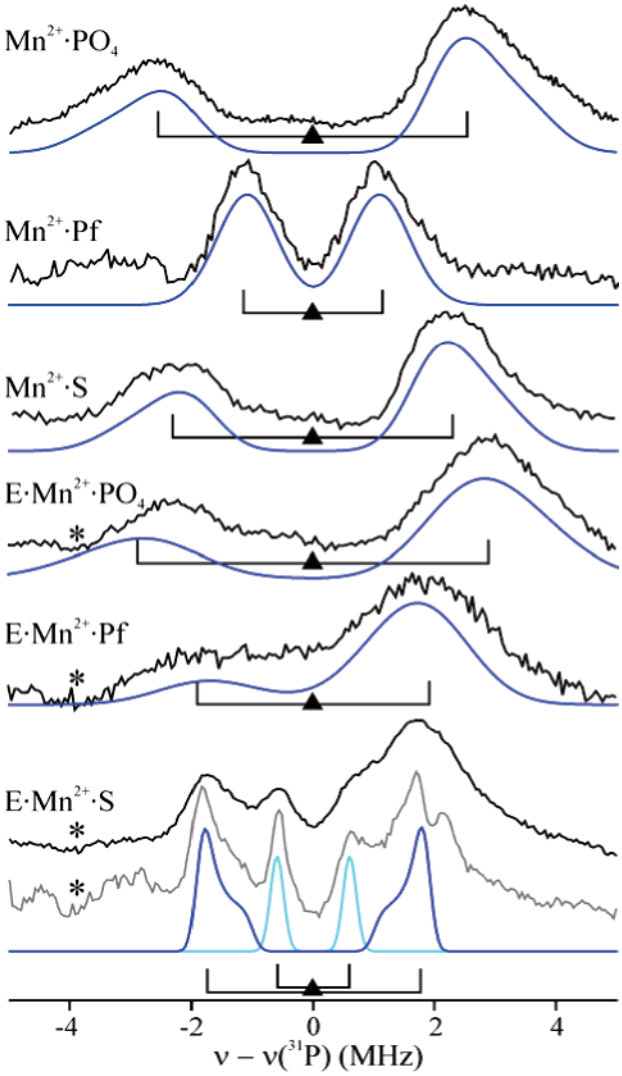


***Figure 2.*** Davies pulsed ENDOR (35 GHz) at $g = 2.0$. Black lines: data collected with 100 kHz RF noise broadening. Gray line: spectrum collected without RF noise broadening. Blue lines: simulations as described in text. Simulated $\nu_+$ and $\nu_-$ peaks have been scaled independently to match experimental data when necessary. The spectrum of E·$Mn^{2+}$·Pf is shown after subtraction of a baseline feature at ~+4 MHz on the scale shown. The baseline spectrum used was that from E·$Mn^{2+}$, which is completely featureless between −5 and +3 MHz. Simulation parameters: $Mn^{2+}$·X, as in Table 1; E·$Mn^{2+}$·$PO_4$ , $r$(Mn−P) = 3.4 Å, $A_{iso}$ = 5.9 MHz, E·$Mn^{2+}$·Pf, as in Table 1, using crystal structure $r$(Mn−P); E·$Mn^{2+}$·S, as in Table 1, all parameters from simulation. Conditions: microwave frequencies as in Figure 1, microwave pulse lengths = 80−40−80 ns, RF pulse length = 60 $\mu$s, number of averaged transients per point: $Mn^{2+}$·$PO_4$, 640; $Mn^{2+}$·S, 1040; $Mn^{2+}$·Pf, 960; E·$Mn^{2+}$·$PO_4$, 3680; E·$Mn^{2+}$·Pf, 4320; E·$Mn^{2+}$·S with noise, 1360; E·$Mn^{2+}$·S without noise 1280. The asterisk (*) indicates the position of an experimental artifact arising from nonlinearity in the RF response that attenuates the ENDOR response around that frequency and causes some spectral distortion, most significantly in the spectrum of E·$Mn^{2+}$·$PO_4$.

samples are shown in Figure 2. Near $g = 2.0$, the ENDOR spectra are completely dominated by nuclear transitions from the $|M_S| = {}^1/_2$ fine-structure levels, and thus, according to eq 1, for each orientation, a pair of peaks from $^{31}P$ ($I = {}^1/_2$, isotopic abundance = 100%) separated by the hyperfine coupling ($A$) is expected. Because the $g$ matrix for $Mn^{2+}$ is nearly isotropic, there can be almost no orientation selection in such spectra, and a $^{31}P$ ENDOR spectrum is a powder pattern composed of statistically weighted contributions from all molecular orientations relative to the external magnetic field (the possible contribution of the zfs to orientation weighting will be discussed later). Such an ENDOR powder pattern for a weakly coupled nucleus with $I = {}^1/_2$ consists of two branches whose center of integrated intensity is at $\nu = \pm A_{iso}/2$ where $A_{iso}$ is the isotropic hyperfine coupling arising from a through-bond transfer of electron spin density from the paramagnetic $Mn^{2+}$ center to the $^{31}P$ of the phosphate/phosphonate.

As described by eq 2, in addition to the $M_S = \pm{}^1/_2$ ENDOR signals, we might expect to see signals from the $M_S = \pm{}^3/_2$ and $\pm{}^5/_2$ fine-structure levels. These were detected in $^1H$ ENDOR experiments (not shown), but due to relaxation effects and S/N limitations, $^{31}P$ signals associated with the higher $M_S$ electron-spin levels were measurable only in E·$Mn^{2+}$·S, and assignment of these peaks was precluded by the overlap of signals from the two types of $^{31}P$ nuclei, baseline effects, and asymmetry in the spectra.

We have simulated the $^{31}P$ ENDOR spectra from all six samples, and the hyperfine parameters are given in Table 1. The uncertainties given in the table are the results of visual comparison of the experimental spectra with a series of simulations with a range of parameters. The spectra have been fitted with a hyperfine tensor composed of a dominant isotropic component, $A_{iso}$, and an axial anisotropic contribution, and thus the hyperfine tensor elements can be written: $A = [A_\perp, A_\perp, A_\parallel] = [A_{iso} - T, A_{iso} - T, A_{iso} + 2T]$. In all cases, $A_{iso} > 3T$, and the $\nu_\pm$ branches each exhibit a peak; these two peaks are separated by $A_\perp$. Disregarding linewidth contributions, each branch has a breadth of $3T/2$. All the spectra of Figure 2, except that of E·$Mn^{2+}$·S, are of this type; this sample shows a signal from a second $^{31}P$ that will be discussed later. Each spectrum has been simulated, as shown in Figure 2,[16] with resulting $A_{iso}$ and $T$ given in Table 1. As Figure 2 and Table 1 show, there is significant variation in the $^{31}P$ hyperfine couplings among the different samples.

The $^{31}P$ hyperfine interaction observed in all of the samples is dominated by $A_{iso}$, which arises from electron spin density in the 3s orbital at the phosphorus nucleus, and reflects the 3s orbital contribution to the phosphorus $3sp^n$ hybrid that is involved in the P−O bond to the oxygen bound to $Mn^{2+}$. As a result, $A_{iso}$ can be written,

$$A_{iso} = A_0\rho_P/(1 + n) \tag{3}$$

where $\rho_P$ is the spin density in the hybrid orbital, $A_0 = 13\,306$ MHz[17] for one electron in the phosphorus 3s orbital, and $n = 3$ for phosphate. The anistropic hyperfine interaction has two contributions:

$$T = T_{loc} + T_{non-loc} \tag{4a}$$

The first of these, $T_{loc}$, can be written in terms of the p orbital contribution to this hybrid,

$$T_{loc} = [n/(1 + n)]T_0\rho_P \tag{4b}$$

where $T_0 = 367$ MHz for one electron in a phosphorus 3p orbital.[17] Even though the spin density on $^{31}P$ is less than 0.05%,[19] the local dipolar interaction is non-negligible in these

(16) Program ENDORSIM written by Peter E. Doan, latest version 2003.
(17) Weil, J. A.; Bolton, J. R.; Wertz, J. E. *Electron Paramagnetic Resonance: Elementary Theory and Practical Applications*; Wiley & Sons: New York, 1994.

systems. The second term in $T$ ($T_{non-loc}$) represents the through-space interaction between the magnetic dipole of the $Mn^{2+}$ ($S = {}^5/_2$) electron spin and the nuclear spin of $^{31}P$ ($I = {}^1/_2$), which is determined by the distance between $Mn^{2+}$ and $^{31}P$, $r$(Mn−P), according to the electron point dipole−nuclear point dipole model:[17]

$$T_{non-loc} = [g_e\beta_e g_N\beta_N/r_{(Mn-P)}{}^3]\rho_{Mn} \quad (4c)$$

where $\rho_{Mn} \approx 1$ is the fractional spin population on $Mn^{2+}$, $g_N$ is the nuclear $g$ factor for $^{31}P = 2.26322$, and the other constant terms have their usual meanings.[17]

Writing the two contributions as the simple sum of eq 4a implies that the local and nonlocal interactions are coaxial. In the case of E·$Mn^{2+}$·X, the crystal structure gives a Mn−P−O angle for the coordinated phosphate/phosphonate of ∼30°, which is equal to the angle between the unique value of $T_{non-loc}$ that lies along the Mn−P vector and that of $T_{loc}$, arising from spin density in the $sp^3$ orbital contributing to the P−O bond whose unique value lies along the O−P bond. We have calculated the rhombic $T$ that arises from the vector sum of the noncoaxial dipolar tensors and used this in simulations. However, the difference in the simulations arising from this correction is small (barely resolvable within the ENDOR linewidth) and would lead, at most, to underestimation of $r$(Mn−P) by 0.1 Å.

For those samples where the dipolar hyperfine pattern of the $\nu_\pm$ branches is resolved and gives a well-defined value for $T$ (Figure 2: $Mn^{2+}$·$PO_4$; $Mn^{2+}$·S; E·$Mn^{2+}$·S (more strongly coupled P)), it is possible to determine the value of $r$(Mn−P) from $T_{non-loc}$ (eq 4c), obtained by combining eqs 3 and 4b, to obtain an equation for $T_{loc}$ in terms of $A_{iso}$,[18]

$$T_{loc} = n(A_{iso}/A_0)T_0 \quad (5)$$

and then subtracting $T_{loc}$ from $T$ (eq 4b). In the cases where the dipolar pattern is not resolved (Figure 2: $Mn^{2+}$·Pf; E·$Mn^{2+}$·$PO_4$; E·$Mn^{2+}$·S (less strongly coupled P); E·$Mn^{2+}$·Pf), we determined, via simulation, an upper limit for $T$ from the width of each ENDOR branch (which is equal at most to $3T/2$); from eq 4c this yields a lower limit for $r$(Mn−P). In the case of $Mn^{2+}$·Pf, we assumed that the intrinsic linewidth was the same as for the other $Mn^{2+}$·X and then systematically increased $T$ until the simulation no longer matched the experimental data. The same approach was used for E·$Mn^{2+}$·S (weaker coupling), but in this case the intrinsic linewidth was assumed to be the same as E·$Mn^{2+}$·S (stronger coupling). For E·$Mn^{2+}$·$PO_4$ and E·$Mn^{2+}$·Pf, the spectra were simulated with a range of input parameters until the combination with the maximum value of $T$ and minimum value of the linewidth consistent with the experimental data was determined.

Figure 2 overlays the $^{31}P$ ENDOR spectrum of $Mn^{2+}$·$PO_4$ with the excellent simulation based on the parameters listed in Table 1, which correspond to $r$(Mn−P) = 3.4(2) Å. To establish the accuracy of the derived $r$(Mn−P), we made comparisons with crystal structures of relevant $Mn^{2+}$ complexes. As there are no crystal structures of $Mn^{2+}$ with only aqua and phosphate ligand(s), we averaged Mn−(O)−P distances in octahedral $Mn(II)O_6$ complexes with at least one phosphate group coordinated, as listed by the November 2003 release of the Cambridge Structural Database (CSD). This distance, $r$(Mn−P) ≈ 3.4 Å, agrees with the value for $r$(Mn−P) established by simulation of the ENDOR spectra.[20]

$Mn^{2+}$·S has a very similar spectrum that can be simulated with a small decrease in both the isotropic and dipolar hyperfine couplings obtained for $Mn^{2+}$·$PO_4$. The decreased value of $A_{iso}$ correlates with a decreased $T_{loc}$ (eq 4c); as a result, $T_{non-loc}$ is very close to that for $Mn^{2+}$·$PO_4$ and $r$(Mn−P) is the same within experimental uncertainty. The $^{31}P$ ENDOR spectra of $Mn^{2+}$·Pf do not show powder line shapes determined by the anisotropic coupling. Rather, they are a doublet split by $A_{iso}$, with each partner line exhibiting a Gaussian line shape; the anisotropic coupling is smaller and unresolved within the intrinsic ENDOR linewidth. Correspondingly, $A_{iso}$ for $Mn^{2+}$·Pf is only ∼60% that of $Mn^{2+}$·$PO_4$, indicating that the interaction of Pf with $Mn^{2+}$ is quite different.

We next consider the ENDOR spectra of these small molecules bound to the enzyme. The crystal structures and thus $r$(Mn−P) values for all the enzyme samples are available.[4,8] Thus we have derived $r$(Mn−P) values directly from simulations of the ENDOR spectra, as with the $Mn^{2+}$·X samples, and compared these results with the crystallographic $r$(Mn−P) values.

The $^{31}P$ spectrum of E·$Mn^{2+}$·$PO_4$ has a similar overall splitting to that of $Mn^{2+}$·$PO_4$, and hence the isotropic coupling is similar; however, in the case of E·$Mn^{2+}$·$PO_4$ the dipolar coupling is not resolved. The best simulation for E·$Mn^{2+}$·$PO_4$ employs parameters similar to those for $Mn^{2+}$·$PO_4$ (Table 1); the minimum value of $r$(Mn−P) = 3.1 Å is consistent with a similar distance between the phosphate and the $Mn^{2+}$ center in each case. As will be discussed below, the minimum value of $r$(Mn−P) from the fitting of the ENDOR data is significantly longer (0.7 Å) than that reported from the crystal structure (see Table 1).

The enzyme in the presence of substrate (E·$Mn^{2+}$·S) exhibits two $^{31}P$ doublets, the most widely split of which can be assigned to coordinated phosphonate. The hyperfine splitting has an isotropic component (−3.15 MHz) that is intermediate in magnitude between that observed in $Mn^{2+}$·S and that in $Mn^{2+}$·Pf. The second doublet has a much smaller isotropic splitting (1.20 MHz) and a dipolar component that is not resolved. This second signal cannot be associated with the EPR transition between other $M_S$ levels because the observed coupling would be larger, rather than smaller, than that associated with the central transition (eq 1). Possible explanations for this signal are discussed later. The spectra collected without RF broadening reveal distinctive line shapes arising from an almost completely axial dipolar interaction where $T_\perp$ is larger than $T_\parallel$ (Figure 2). This requires that $T_{non-loc}$ have a sign opposite from $A_{iso}$ and, according to eq 5, also from $T_{loc}$.[21]

(18) Manikandan, P.; Choi, E.-Y.; Hille, R.; Hoffman, B. M. *J. Am. Chem. Soc.* **2001**, *123*, 2658−2663.

(19) The unpaired electron spin density in the phosphorus 3s orbital is calculated from $A_{iso}/A_0$ where $A_0(^{31}P) = 13\,307$ MHz. Our calculations, by analogy with previous work,[18] do not include separately the contribution of core s electron density (1s, 2s). If a portion of $A_{iso}$ is derived from spin density on 1s and 2s orbitals then, from eq 3, the value of $T_{loc}$ will be somewhat overestimated. This in turn will lead to an underestimation of $T_{non-loc}$ and consequently a value of $r$(Mn−P) that is too small. Our calculations of $r$(Mn−P) for E·$Mn^{2+}$·X agree, within experimental uncertainty, with the X-ray-derived distances.

(20) The calculation takes into account modest covalency of metal−ligand bonds, by use of 90% spin localization on $Mn^{2+}$. A change in covalency of ±10% changes the calculated $r$(Mn−P) values by ca. ±0.1 Å.

(21) The absolute signs of $A_{iso}$, $T_{loc}$, and $T_{non-loc}$ cannot be determined by these measurements, and thus $A_{iso}$ is arbitrarily assigned as negative. However, their relative signs are internally consistent.

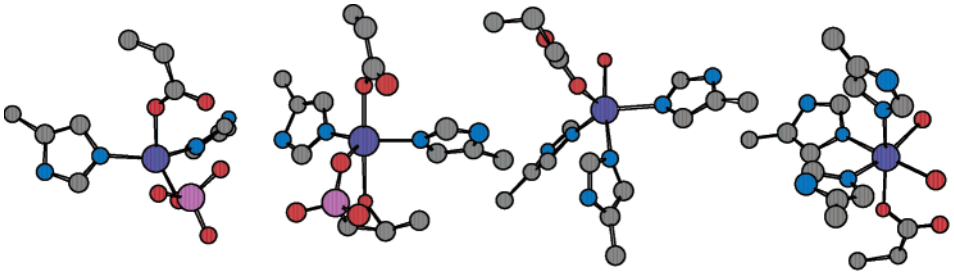


***Figure 3.*** Mononuclear $Mn^{2+}$ enzyme active sites with four-, five-, and six-coordination as determined by X-ray crystallography of FosA,[4] cambialistic SOD,[39] and barley oxalate oxidase.[25]

E·$Mn^{2+}$·Pf has an isotropic coupling very similar to that from E·$Mn^{2+}$·S and almost twice that observed in $Mn^{2+}$·Pf. The contribution to the lineshape from $T$ is obscured by a large ENDOR linewidth. Given that the crystal structures indicate chelation by Pf, as is the case with fosfomycin, we anticipate that the spin polarization characteristics will be similar. Therefore, we assume that $A_{iso}$ has the sign opposite to that of $T_{non-loc}$ and with this we arrive at $^{31}$P parameters very similar to those from E·$Mn^{2+}$·S[22] and a minimum value of $r$(Mn−P) that is consistent with the crystal structure (Table 1).

## Discussion

We first discuss the correlation between the zfs parameters determined by EPR and the $Mn^{2+}$ coordination geometry. We then discuss the correlation between the $^{31}$P hyperfine coupling parameters determined by pulsed ENDOR and the binding modes of small molecules (substrate/inhibitor) to the $Mn^{2+}$ active site of PA1129 FosA.

**EPR and Coordination Geometry.** Previous CW EPR studies of FosA followed a long tradition of using the zfs parameters of a $Mn^{2+}$ center to infer its coordination number and substrate binding modes.[7] Historic correlations of zfs with geometry, however, were based on $Mn^{2+}$ sites with close to ideal symmetries—octahedral or tetrahedral—and ligands with "cylindrically symmetric" $\pi$-bonding (halide or oxide donors, for which $\pi_{||} \approx \pi_{\perp}$).[23,24] The recent determination of crystal structures for a number of $Mn^{2+}$ metalloenzymes and $Mn^{2+}$ complexes now reveals that predictions of coordination number and geometry of $Mn^{2+}$ sites based on zfs parameters are *not* robust. The crystal structure of barley oxalate oxidase[25] displays an octahedral $Mn^{2+}$ with 3N, 3O coordination (Figure 3) and an EPR signal typical of $Mn^{2+}$ with small zfs (values of $D$, $E$ not stated but clearly small).[26] In contrast, $Mn^{2+}$ bis(2-pyridylmethyl)amine has a 6N octahedral coordination environment, but single-crystal EPR studies show that its zfs parameters are large in magnitude: $D = -0.2190$ and $E = 0.0058$ cm$^{-1}$.[27] Cambialistic superoxide dismutase from *Porphyromonas gingivalis* contains five-coordinate $Mn^{2+}$ [28] (Figure 3), as in FosA with substrate or Pf, and high-field/frequency EPR (HFEPR) studies indicate relatively large zfs values: $|D| = 0.3562$ and $|E| = 0.0068$ cm$^{-1}$.[28] However, HFEPR of six-coordinate *trans*-Mn(*o*-phenanthroline)$_4$X$_2$ (4N, 2X; X = Cl, Br, I) yielded $|D| = 0.359$ for X = Br;[29] essentially the same value as for the five-coordinate enzyme active site. Moreover, the magnitude of both $D$ and $E$ is sensitive to the nature of the nitrogen donor (*o*-phenanthroline or $\gamma$-picoline) and extremely sensitive to the halide ligand. The difficulty of correlating zfs parameters with coordination chemistry has also been pointed out in a very thorough recent HFEPR study of a series of $Mn^{2+}$ complexes of 2,2′:6′,2″-terpyridine.[30]

Indeed, the present results again demonstrate that the *identity* of the $Mn^{2+}$ ligands can have a greater effect on the values of $D$ and $E$ than does the coordination *number*. Thus, simulation of the ESE-EPR spectra gave similar values of $D$ and $E$ for E·$Mn^{2+}$·$PO_4$ and E·$Mn^{2+}$·Pf (Figure S5), yet the crystal structures reveal that E·$Mn^{2+}$·$PO_4$ has a highly distorted tetrahedral $Mn^{2+}$ coordination environment while E·$Mn^{2+}$·Pf exhibits a five-coordinate, highly symmetric trigonal bipyramidal ligand arrangement. Further, E·$Mn^{2+}$·Pf and E·$Mn^{2+}$·S have very similar coordination environments, but $D$ and $E$ are dramatically larger for E·$Mn^{2+}$·S. Clearly, zfs parameters for the $Mn^{2+}$ ($S = {}^5/_2$) ion cannot be readily correlated to the coordination number and geometry, despite the temptation to do so and the long history of such attempts.

**$^{31}$P ENDOR.** There are several reports of $^{31}$P ENDOR experiments on phosphate−metal interactions in biological systems, almost all of which used CW techniques to probe the bonding of metal ions to nucleotides and nucleic acids. Of direct relevance here are the X-band CW experiments on $Mn^{2+}$ in the oxalate−ATP complex of pyruvate kinase[31] and the 35 GHz CW studies of the $Mn^{2+}$ site in the hammerhead ribozyme.[32] In both cases, $^{31}$P couplings of ~4 MHz for phosphate directly coordinated to the $Mn^{2+}$ ion were within the range of couplings reported here.[33] In comparison with the CW spectra of those studies, the Davies pulsed spectra reported here provide dramatically better resolution of the $^{31}$P hyperfine peaks,

(22) A satisfactory simulation can also be obtained with $A_{iso}$ and $T_{non-loc}$ having the same sign.
(23) Hempel, J. C.; Palmer, R. A.; Yang, M. C. L. *J. Chem. Phys.* **1976**, *64*, 4314−4320.
(24) Sharma, R. R. *Phys. Rev. B: Solid State* **1970**, *[3]2*, 3316−3318.
(25) Woo, E.-J.; Dunwell, J. M.; Goodenough, P. W.; Marvier, A. C.; Pickersgill, R. W. *Nat. Struct. Biol.* **2000**, *7*, 1036−1040.
(26) Whittaker, M. M.; Whittaker, J. W. *J. Biol. Inorg. Chem.* **2002**, *7*, 136−145.
(27) Glerup, J.; Goodson, P. A.; Hodgson, D. J.; Michelsen, K.; Nielsen, K. M.; Weihe, H. *Inorg. Chem.* **1992**, *31*, 4611−4616.
(28) Un, S.; Tabares, L. C.; Cortez, N.; Hiraoka, B. Y.; Yamakura, F. *J. Am. Chem. Soc.* **2004**, *126*, 2720−2726.
(29) Lynch, W. B.; Bourse, R. S.; Freed, J. H. *J. Am. Chem. Soc.* **1993**, *115*, 10909−10915.
(30) Mantel, C.; Baffert, C.; Romero, I.; Deronzier, A.; Pécaut, J.; Collomb, M.-N.; Duboc, C. *Inorg. Chem.* **2004**, *43*, 6455−6463.
(31) Tan, X.; Poyner, R.; Reed, G. H.; Scholes, C. P. *Biochemistry* **1993**, *32*, 7799−7810.
(32) Morrissey, S. R.; Horton, T. E.; DeRose, V. J. *J. Am. Chem. Soc.* **2000**, *122*, 3473−3481.
(33) In agreement with these results, X-band ESEEM studies of adenine nucleotide binding to a Mn-substituted $Mg^{2+}$−protein, F1-ATPase, showed modulation assigned to $^{31}$P with hyperfine coupling of 4.5 ± 0.1 MHz: Zoleo, A.; Contessi, S.; Lippe, G.; Pinato, L.; Brustolon, M.; Brunel, L.-C.; Dabbeni-Sala, F.; Maniero, A. L. *Biochemistry* **2004**, *43*, 13214−13224.

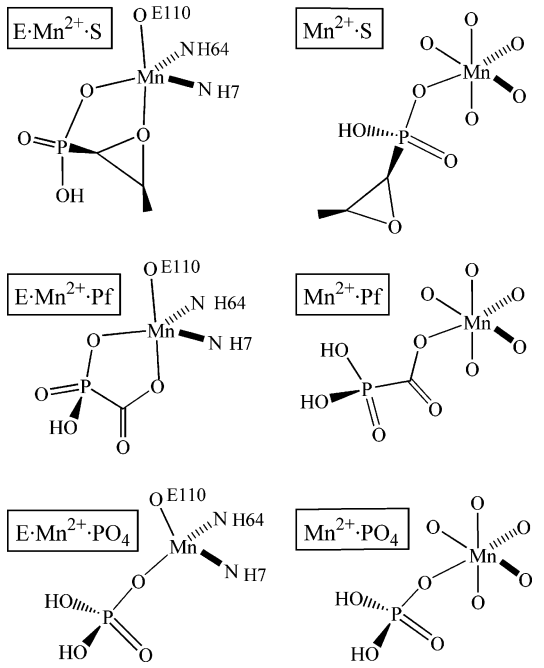


***Figure 4.*** Phosphate/phosphonate binding modes as determined by X-ray crystal structures[4,8] and $^{31}$P ENDOR studies. The degree of protonation shown for the P-containing molecules is not meant to be definitive; hydrogen atoms on the aqueous $Mn^{2+}$ are not shown. Unidentate coordination for the carboxylate in $Mn^{2+}$·Pf is shown but is not experimentally determined.

allowing analysis of the dipolar component of the hyperfine interaction. In our experience, 35 GHz pulsed $^{31}$P ENDOR experiments on $Mn^{2+}$·X produce data with high S/N in a single 3 min scan, while 35 GHz CW experiments on the same samples demand a 20-fold longer collection time even to produce distorted, lower S/N $^{31}$P peaks.

There are two previous reports of the application of pulsed ENDOR techniques to measure metal−$PO_4$ interactions in biochemical systems,[34,35] but those studies are not directly comparable to the present study. In both cases, little or no isotropic $^{31}$P hyperfine coupling was observed, and the signals were thus assigned to outer-sphere nucleotide phosphates; one case involved DNA binding to a Co(II)-substituted Zn finger protein.[35] To our knowledge, the present article describes the first use of pulsed $^{31}$P ENDOR to study phosphates (and phosphonates) directly coordinated to a metal center in a biological system.

Comparisons of the $^{31}$P coupling for phosphate bound to $Mn^{2+}$ in the protein samples with the couplings from $Mn^{2+}$·X have enabled us to determine how the enzyme cavity modifies the manganese coordination environment. Figure 4 shows a schematic representation of the X-ray-derived coordination in E·$Mn^{2+}$·X and the coordination in the equivalent $Mn^{2+}$·X samples as is now inferred from the ENDOR data.

**Phosphate Coordination.** E·$Mn^{2+}$·$PO_4$ and $Mn^{2+}$·$PO_4$ have similar values for $A_{iso}$ (Table 1), which implies that the bonding in the two cases is very similar. Phosphate has unidentate coordination to $Mn^{2+}$ in the enzyme. However, the crystallographic study reported a surprisingly short Mn−O bond (1.785 Å) and thus a value, $r$(Mn−P) = 2.494 Å, which likely is too small.[4] An analysis of the more than 150 $Mn^{2+}$ complexes reported in the CSD with formula $MnO_n$ where $n$ = 5, 6, 7, 8 has determined that the Mn−O bond lengths average 2.2 Å with a minimum of 1.98 Å.[36] Likewise, our analysis of the far fewer four-coordinate $Mn^{2+}$ complexes with at least one oxophosphorus donor ligand indicates that the average Mn−O−(P) bond distance is 2.0 Å and the average Mn−(O)−P distance is 3.3 Å. The ENDOR analysis yields an average $PO_4$ position with $r$(Mn−P) = 3.2 Å, in agreement with the small-molecule crystallographic data. We suggest that the Mn−(O)−P distance in the crystal structure of E·$Mn^{2+}$·$PO_4$ is underestimated, as a result of disorder in the coordinated $PO_4$. Disorder of the coordinated phosphate is consistent with the $^{31}$P ENDOR spectra where the $\nu_+$ peak has a large linewidth (1.8 MHz) and is almost Gaussian-shaped, indicative of a distribution of orientations and distances.

Indeed, the conclusions of ENDOR and small-molecule studies are not incompatible with the protein crystallography. The best explanation of the electron density near the Mn in the crystal structure of the phosphate complex was obtained with two partially occupied phosphate sites in each subunit that were refined with occupancies of 0.60 and 0.35, respectively. The $r$(Mn−P) for the secondary sites are 3.33 Å for one subunit and 3.17 Å in the other,[4] which is an average in excellent agreement with the ENDOR-derived distance.

**Substrate Coordination.** Considering now complexes of substrate, the crystal structure of E·$Mn^{2+}$·S shows that the $Mn^{2+}$ is five-coordinate with nearly perfect trigonal bipyramidal geometry: the oxirane oxygen of the substrate is located at one of the apical sites; the phosphate oxygen and histidine nitrogens make up the equatorial plane. The reported Mn−oxirane oxygen distance (2.350 Å) is somewhat longer than expected for a five-coordinate $Mn^{2+}$ complex[36] presumably because of the poorer electron-donating ability of this oxygen.

Considering the ENDOR characterization of *S* binding to $Mn^{2+}$, $A_{iso}$ for $Mn^{2+}$·S is ∼14% smaller than that for $Mn^{2+}$·$PO_4$, suggesting slightly weaker bonding of phosphonate to $Mn^{2+}$, as might be expected for the less ionic phosphonate ligand.

However, $A_{iso}$ for E·$Mn^{2+}$·S is ∼40% smaller in magnitude than that for $Mn^{2+}$·S, and the sign of the coupling is reversed, demonstrating that enzyme binding has a large effect on the interaction between fosfomycin and $Mn^{2+}$. The decrease in magnitude suggests that spin density on the phosphonate $^{31}$P has been reduced and has instead been distributed onto the oxirane O. The sign change requires a change in spin polarization at the $^{31}$P nucleus, which, in a simplified model, can result from a change by one in the number of $\sigma$ bonds in the delocalization pathway. This suggests that the major pathway for transfer of spin density to the phosphorus may occur via the oxirane oxygen (i.e., via Mn−$O_{(oxirane)}$−C−P) rather than via the coordinated, phosphonate oxygen (i.e., via Mn−O−P).

As described above, $^{31}$P ENDOR spectra of E·$Mn^{2+}$·S show a second set of peaks with an isotropic splitting less than half that of the coupling from the metal-bound substrate. We have suggested that this arises from a second "outer-sphere" substrate molecule nearby, but there are several possible alternative interpretations.

(34) Hoogstraten, C. G.; Grant, C. V.; Horton, T. E.; DeRose, V. J.; Britt, R. D. *J. Am. Chem. Soc.* **2002**, *124*, 834−842.
(35) Walsby, C. J.; Krepkiy, D.; Petering, D. H.; Hoffman, B. M. *J. Am. Chem. Soc.* **2003**, *125*, 7502−7503.
(36) Palenik, G. J. *Inorg. Chem.* **1997**, *36*, 4888−4890.

The first explanation is that all of the ENDOR pattern arises from the phosphonate $^{31}$P of a single, directly coordinated fosfomycin molecule. There are two possible alternatives: (i) ENDOR involving multiple electron spin manifolds, (i.e., $|S, M_S\rangle = |^5/_2, \pm^5/_2\rangle \leftrightarrow |^5/_2, \pm^3/_2\rangle$ and $|^5/_2, \pm^3/_2\rangle \leftrightarrow |^5/_2, \pm^1/_2\rangle$ in addition to $|^5/_2, \pm^1/_2\rangle \leftrightarrow |^5/_2, \mp^1/_2\rangle$) and (ii) ENDOR involving multiple relative orientations of the nuclear, $g$, and $D$ matrix coordinate systems with respect to the external magnetic field.

(i) One could imagine that the more weakly coupled peaks are associated with the $M_S = \pm^1/_2$ from the interaction of the levels of the $Mn^{2+}$ ion and that the larger couplings are associated with $|M_S| > {}^1/_2$ transitions, as described by eq 1. However, we would expect the ENDOR intensity involving the higher $|M_S|$ manifolds to be relatively insignificant in the $g \approx 2$ region as the EPR intensity of these higher transitions is much less than that of the $|\pm^1/_2\rangle \leftrightarrow |\mp^1/_2\rangle$ signals in this region. Instead, the more weakly coupled peaks in the $^{31}$P ENDOR from E·$Mn^{2+}$·S are actually less intense than the outer peaks. Further, the small $A_{iso}$ and the narrow width of the peaks, implying a small value of $T$, demonstrate that the inner peaks cannot be from a phosphonate directly coordinated to the metal.

(ii) To test whether orientational effects within the $|\pm^1/_2\rangle \leftrightarrow |\mp^1/_2\rangle$ signals lead to multiple signals as a function of applied field ($g$ value), we have collected additional $^{31}$P ENDOR across the entire $|\pm^1/_2\rangle \leftrightarrow |\mp^1/_2\rangle$ region ($1.8 < g_{obs} < 2.2$) to probe the effect of orientation selection derived from the zfs tensor (Figure S7). Only small variations are observed in the positions of the lines in the $^{31}$P ENDOR. This implies that both sets of signals are "powder averages" associated with an isotropic $g$ value on the $|M_S| = {}^1/_2$ levels and thus cannot arise from a single $^{31}$P.

We conclude that the second doublet is associated with a second fosfomycin bound near to the active site. The additional signal could, in principle, arise from another fosfomycin molecule in the same general location, but with a different mode of coordination, similar to the disorder observed crystallographically for the phosphate,[4] as mentioned above. For example, weaker $^{31}$P coupling might occur upon coordination of the oxirane oxygen without coordination of a phosphonate oxygen. However, it seems implausible that there would be such nonspecific binding of substrate at the active site of an enzyme. Indeed, in contrast to the phosphate complex crystal structure, that of the fosfomycin complex at a resolution of 1.19 Å reveals no indication of a second inner-sphere orientation of the substrate or other phosphorus species that might give rise to the weakly coupled ENDOR signal.

We therefore suggest that the signal instead is associated with a "second-shell" $^{31}$P nucleus located further from the $Mn^{2+}$ than that of the primary substrate molecule. Although the dipolar contribution to the $^{31}$P hyperfine interaction is not resolved within the ENDOR linewidth, we have determined a minimum value of $r$(Mn−P) of 5.6 Å, which correlates with the crystal structure of E·$Mn^{2+}$·S that shows a second ("outer-sphere") substrate molecule close to the ("inner-sphere") fosfomycin coordinated to the active site (Figure 5). This outer-sphere molecule exhibits well-defined electron density with a higher average B-factor (30.6 Å$^2$) than that of the inner-sphere molecule (15.0 Å$^2$). However, the phosphonate groups of both are very well defined in the structure with average B-factors for the phosphorus atoms of 19.8 and 14.4 Å$^2$ for the outer-sphere and inner-sphere molecules, respectively. The occupancy of the outer-sphere binding site is probably the result of the high concentration of fosfomycin used in the crystallographic and magnetic resonance experiments. The specific binding site of the outer-sphere fosfomycin may be due to very favorable hydrogen-bonding interactions between the phosphonate and the ammonium group of Lys90 and the guanidinium group of Arg93. It is possible that this site may be part of a cationic pathway for substrate approach to the $Mn^{2+}$ center.

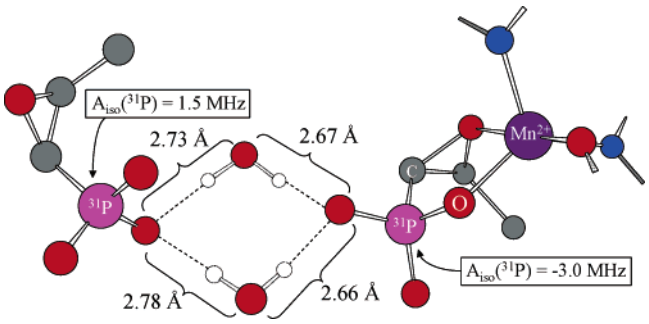


***Figure 5.*** Proposed hydrogen bonding pathway for electron spin density to $^{31}$P of second fosfomycin substrate molecule. Atomic coordinates as reported by Rife et al.[4] Hydrogens atoms are positioned so as to minimize the P−O−H−O path length.

Although $A_{iso}$ for this second $^{31}$P is substantially smaller than that of the inner-sphere substrate molecule, it is still much larger than might be anticipated given the distance from $Mn^{2+}$ (9.08 Å). However, the observation of a $^{31}$P isotropic hyperfine interaction derived from spin density transferred over a large distance is not unprecedented.[37] In this case, the relatively large $A_{iso}$($^{31}$P) from the outer-sphere fosfomycin might be explained by the nature of the hydrogen bonding *between* the two substrate molecules. As shown in Figure 5, the crystal structure reveals two water molecules located between the phosphonate oxygens of each fosfomycin. These water molecules are arranged in a highly symmetric fashion with respect to the closest phosphonate oxygens, which suggests a H-bonding pathway for transfer of spin density to the phosphorus nucleus.[38]

**Phosphonoformate Coordination.** $A_{iso}$ for $Mn^{2+}$·Pf is less than half that for $Mn^{2+}$·S (Table 1). This suggests that, in aqueous solution, Pf does not bind via the phosphonate; only the formate group of Pf is coordinated to $Mn^{2+}$ (Figure 4). As a result, the isotropic coupling is derived from transmission of spin density to the phosphonate P via the $\sigma$-bonding framework Mn−$O_{formate}$−C−P, rather than directly via Mn−O−P. In contrast, the crystal structure of E·$Mn^{2+}$·Pf indicates that here the Pf chelates to the $Mn^{2+}$ via the phosphonate and carboxylate groups. The Mn−O bond to the carboxylate is shorter than that to the oxirane in E·$Mn^{2+}$·S and at 2.232 Å is closer to that expected for typical five-coordinate $Mn^{2+}$.[36] As with the coordination of the substrate, $A_{iso}$ is significantly reduced compared with coordinated phosphate, in this case likely reflecting delocalization of spin density onto the carboxylate

(37) Pulsed $^{31}$P 35 GHz ENDOR measurements of the Co(II)-substituted Zn-finger protein with bound DNA indicated $A_{iso}$($^{31}$P) = 0.24 MHz arising from the $^{31}$P of the nearest DNA phosphodiester which, from the crystal structure, is located 8.3 Å from the metal center.[35]

(38) The $O_{(distant\ substrate)}$−$O_{(water)}$−$O_{(coordinated\ substrate)}$ dihedral angles of 98.6° and 99.5° are close to that for water (104.5°) and combined with the short $O_{(substrate)}$−$O_{(water)}$ bond distances (2.67−2.78 Å) suggest strong H-bonding by the two water molecules, as diagramed in Figure 5.

(39) Sugio, S.; Hiraoka, B. Y.; Yamakura, F. *Eur. J. Biochem.* **2000**, *267*, 3487−3495.

of Pf. Given that Pf coordination is similar to that of substrate, we have assumed the same polarization of the spin density at the phosphorus and with this model obtain hyperfine parameters very similar to those for $E{\cdot}Mn^{2+}{\cdot}S$. The change in spin polarization pathway is the cause of the difference in sign of $A_{iso}$ for $Mn^{2+}{\cdot}Pf$ relative to $E{\cdot}Mn^{2+}{\cdot}Pf$, as described above for $E{\cdot}Mn^{2+}{\cdot}S$ and $Mn^{2+}{\cdot}S$.

## Conclusions

FosA is inherently important from medical and biological points of view, but it also serves as an excellent testing ground for the use of spectroscopic techniques to determine details of the coordination of phosphates and phosphonates. With the publication of the crystal structures of $E{\cdot}Mn^{2+}{\cdot}S$, $E{\cdot}Mn^{2+}{\cdot}Pf$, and $E{\cdot}Mn^{2+}{\cdot}PO_4$, we have been able to compare the ability of ESE-EPR and pulsed $^{31}P$ ENDOR techniques to measure the ligand binding modes and bonding characteristics.

The high resolution and signal-to-noise available from the pulsed $^{31}P$ ENDOR, as compared with that of CW ENDOR experiments, have proven extremely useful in probing the details of the binding of phosphates and phosphonates to $Mn^{2+}$. Not only has this allowed an accurate measurement of $A_{iso}$, which gives information on $Mn^{2+}-P$ bonding covalency, but also critically permits an analysis of the through-space component of the hyperfine coupling and, thus, direct information on Mn−P distances. Comparison of the isotropic and dipolar components of the $^{31}P$ hyperfine coupling has allowed us to determine how the environment in the enzyme pocket influences coordination of the guest molecules (X) by comparison with their coordination to aqueous $Mn^{2+}$. For $X = PO_4$, coordination is very similar in both cases; for X = Pf, coordination is modified from carboxylate-only binding in free solution to chelation via the phosphonate in enzyme; for X = S (fosfomycin), phosphonate-only binding in free solution is modified to chelation with the oxirane O in enzyme.

Earlier CW EPR experiments on FosA were misled by forbidden transitions that appear at relatively high microwave powers and possibly by sample preparation issues as well. ESE-EPR has the advantage over CW EPR in having good S/N for what corresponds to CW spectra with very low microwave power. Both EPR techniques show that absorption-display spectra are far more revealing than the conventional derivative display for revealing the details of fine structure transitions in high-spin $Mn^{2+}$. From the ESE-EPR spectra reported here, we have determined the zfs parameters of the $Mn^{2+}$ centers studied. However, our results, combined with those for various $Mn^{2+}$ complexes and other metalloenzymes, have disclosed that it is not possible to determine the coordination number and geometry for $Mn^{2+}$ complexes solely by analysis of these zfs parameters.

We anticipate that the use of pulsed $^{31}P$ ENDOR techniques will find wide application in understanding the coordination of $Mn^{2+}$ to phosphorus-containing biological metal centers such as small molecules, proteins, and perhaps most notably in studies of the binding of metal ion to DNA and nucleic acids.

**Acknowledgment.** This work was supported by NIH Grants R01 AI42756, T32 GM65086, P30 ES00267 (R.N.A.), and HL13531 (B.M.H.). We thank Dr. Peter E. Doan and the reviewers for helpful suggestions.

**Supporting Information Available:** Figures S1−S7 showing CW 35 GHz EPR spectra of $E{\cdot}Mn^{2+}{\cdot}X$, effect of experimental conditions on ESE-EPR spectrum of $E{\cdot}Mn^{2+}{\cdot}S$, and field-dependent $^{31}P$ Davies ENDOR spectra of $E{\cdot}Mn^{2+}{\cdot}S$. This material is available free of charge via the Internet at http://pubs.acs.org.

JA044094E